



HAL
open science

Influence of enhanced melt supply on upper crustal structure at a mid-ocean ridge discontinuity: A three-dimensional seismic tomographic study of 9°N East Pacific Rise

C. H. Tong, P. J. Barton, R. S. White, M. C. Sinha, S. C. Singh, J. W. Pye, R. W. Hobbs, S. Bazin, A. J. Harding, G. M. Kent, et al.

► To cite this version:

C. H. Tong, P. J. Barton, R. S. White, M. C. Sinha, S. C. Singh, et al.. Influence of enhanced melt supply on upper crustal structure at a mid-ocean ridge discontinuity: A three-dimensional seismic tomographic study of 9°N East Pacific Rise. *Journal of Geophysical Research*, 2003, 108, pp. 514-520. 10.1029/2002JB002163 . insu-03598409

HAL Id: insu-03598409

<https://insu.hal.science/insu-03598409>

Submitted on 6 Mar 2022

HAL is a multi-disciplinary open access archive for the deposit and dissemination of scientific research documents, whether they are published or not. The documents may come from teaching and research institutions in France or abroad, or from public or private research centers.

L'archive ouverte pluridisciplinaire **HAL**, est destinée au dépôt et à la diffusion de documents scientifiques de niveau recherche, publiés ou non, émanant des établissements d'enseignement et de recherche français ou étrangers, des laboratoires publics ou privés.

Copyright

Influence of enhanced melt supply on upper crustal structure at a mid-ocean ridge discontinuity: A three-dimensional seismic tomographic study of 9°N East Pacific Rise

C. H. Tong,¹ P. J. Barton, R. S. White, M. C. Sinha,² S. C. Singh,³ J. W. Pye,¹ and R. W. Hobbs

Department of Earth Sciences, Bullard Laboratories, University of Cambridge, Cambridge, UK

S. Bazin,³ A. J. Harding, G. M. Kent, and J. A. Orcutt

Cecil H. and Ida M. Green Institute of Geophysics and Planetary Physics, Scripps Institution of Oceanography, University of California, San Diego, California, USA

Received 21 August 2002; revised 22 May 2003; accepted 1 July 2003; published 9 October 2003.

[1] We present a three-dimensional upper crustal model of the 9°03'N overlapping spreading center (OSC) on the East Pacific Rise that assists in understanding the relationship between melt sills and upper crustal structure at a ridge discontinuity with enhanced melt supply at crustal levels. Our *P* wave velocity model obtained from tomographic inversion of ~70,000 crustal first arrival travel times suggests that the geometry of extrusive emplacement are significantly different beneath the overlapping spreading limbs. Extrusive volcanic rocks above the western melt sill are inferred to be thin (~250 m). More extensive accumulation of extrusives is inferred to the west than to the east of the western melt sill. The extrusive layer inferred above the eastern melt sill thickens from ~350 (at the neovolcanic axis) to 550 m (to the west of the melt sill). Volcanic construction is likely to be significant in the formation of ridge crest morphology at the OSC, particularly at the tip of the eastern limb. On the basis of our interpretation of the velocity model, we propose that enhanced magma supply at crustal levels at the OSC may provide an effective mechanism for the migration of ridge discontinuities. This “dynamic magma supply model” may explain the commonly observed nonsteady migration pattern of ridge discontinuities by attributing this to the temporal fluctuations in melt availability to the overlapping spreading limbs. *INDEX TERMS*: 0930 Exploration Geophysics: Oceanic structures; 3025 Marine Geology and Geophysics: Marine seismics (0935); 3035 Marine Geology and Geophysics: Midocean ridge processes; 7220 Seismology: Oceanic crust; *KEYWORDS*: overlapping spreading center, magma supply, ridge segmentation, ridge propagation, crustal evolution, oceanic crust

Citation: Tong, C. H., et al., Influence of enhanced melt supply on upper crustal structure at a mid-ocean ridge discontinuity: A three-dimensional seismic tomographic study of 9°N East Pacific Rise, *J. Geophys. Res.*, 108(B10), 2464, doi:10.1029/2002JB002163, 2003.

1. Introduction

[2] Mid-ocean ridges exhibit a range of morphologic discontinuity structures. *Macdonald et al.* [1991] proposed a hierarchy of ridge discontinuities, dependent on the size of the ridge axis offset. Overlapping spreading centers (OSCs) represent an important class of these discontinuities and are commonly found on fast-spreading and intermediate-spreading rate ridges (>60 mm yr⁻¹). Ridge discontinuities such as OSCs are associated with bathymetric ridge

crests that have a smaller cross-sectional area and deeper bathymetry than the ridge crests elsewhere along ridge segments [e.g., *Macdonald and Fox*, 1983, 1988; *Scheirer and Macdonald*, 1993]. The magma supply model [e.g., *Sempéré and Macdonald*, 1986] is used to explain these along-axis morphologic variations by attributing them to the surficial manifestation of a reduced supply of magma at ridge discontinuities. However, the relationship between magma supply and morphology appears to be more complex than this simple model suggests: geophysical studies at ridge discontinuities show that these localities may also experience unusually high levels of magma supply [e.g., *Collier and Sinha*, 1992; *Kent et al.*, 2000; *Peirce et al.*, 2001; *Day et al.*, 2001]. These investigations have led to a competing geologic model in which magma may be fed more locally to ridge discontinuities [e.g., *Kent et al.*, 2000].

[3] At upper crustal levels, along-axis variation in layer 2A thickness and its relationship with the geometry of melt sills have been the subject of intensive geophysical inves-

¹Now at Department of Earth Science and Engineering, Imperial College London, London, UK.

²Now at Southampton Oceanography Centre, University of Southampton, School of Ocean and Earth Science, Southampton, UK.

³Now at Laboratoire de Géosciences Marines, Institut de Physique du Globe de Paris, Paris, France.

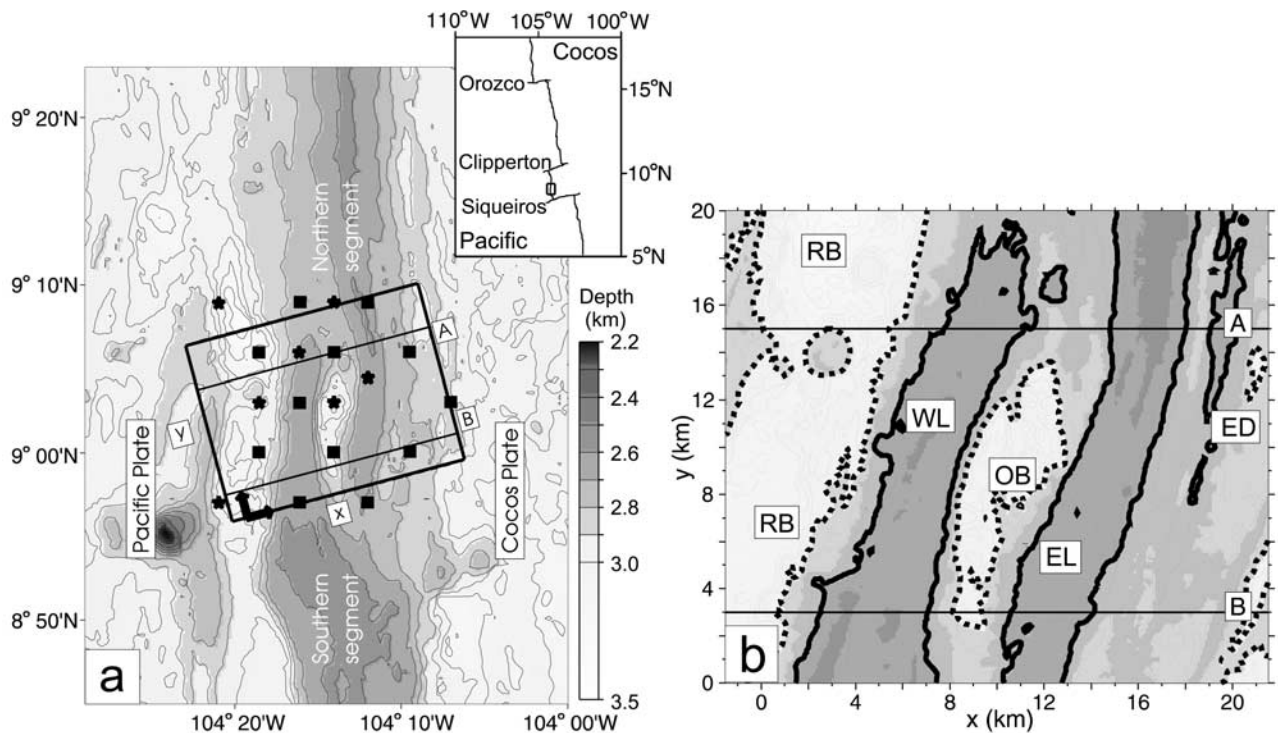


Figure 1. (a) The $9^{\circ}03'N$ overlapping spreading center (OSC) on the East Pacific Rise and the geometry of the ARAD experiment that corresponds to the data used in this study. Inset shows the location of the study area in the East Pacific. Over 160,000 shots from 201 parallel seismic lines within the box ($20 \text{ km} \times 23 \text{ km}$) were recorded by 19 ocean bottom hydrophones and ocean bottom seismometer (solid stars: Cambridge instruments; solid squares: Scripps instruments). Shot locations were determined by Differential Global Positioning System (DGPS) navigation to an accuracy of a few meters. The sampling rate of the Cambridge OBHs/OBS and the Scripps OBHs was 7.8 and 4 ms, respectively. The orthogonal arrows indicate the origin of the local coordinate system. Lines A and B show the locations of the vertical profiles of the velocity models shown in Figure 7. (b) Detailed bathymetric map of the rotated box in Figure 1a. The origin of the local coordinate system is at $104.307420^{\circ}W$, $8.939218^{\circ}N$. Principal morphologic regions of the OSC are shown: RB, relict basin; WL, western limb; OB, overlap basin; EL, eastern limb; and ED, eastern discordant zone. Lines A and B show the same profiles as in Figure 1a. The thick solid line indicates the bathymetric ridge crests ($<2700 \text{ m}$), whereas the dotted lines define the basins ($>2900 \text{ m}$).

tigations [e.g., Kent et al., 1993a, 1993b; Hooft et al., 1996; Tolstoy et al., 1997; Carbotte et al., 2000]. These studies provide constraints on the crustal emplacement mechanism, linking the along-axis variation in the characteristics of melt sills to the features of the extrusives and the ridge crest morphology. The contrast between on-axis and off-axis upper crustal structures has also been investigated extensively, leading to models that describe the age dependence of characteristics of upper crustal seismic layers [Toomey et al., 1990, 1994; Vera et al., 1990; Harding et al., 1993; Christeson et al., 1994; Carbotte et al., 1997, 2000; Carlson, 1998]. However, our understanding of the influence of a melt sill on the upper crustal structure has been based mainly on these studies of midsegments away from major ridge discontinuities.

2. Geologic Setting and Motivation

[4] The $9^{\circ}03'N$ OSC on the East Pacific Rise is the major ridge discontinuity located along the ridge axis between the Clipperton Transform and the Siqueiros Trans-

form (Figure 1a), consisting of two spreading limbs that overlap by 27 km. An overlap basin separates the spreading limbs by 8 km (Figure 1b). The eastern limb and the OSC are generally propagating southward [Carbotte and Macdonald, 1992]. The western limb undergoes self-decapitation, in which the ridge crest rotates anticlockwise and is eventually cut off from the main ridge segment to its south, resulting in the relict basins and relict limbs in the western discordant zone [Macdonald et al., 1987; Carbotte and Macdonald, 1992]. Anomalously wide melt sills are imaged under the spreading limbs of the OSC [Kent et al., 2000; Tong et al., 2002]. The melt sill beneath the western limb (the western melt sill) is up to $\sim 2.5 \text{ km}$ wide, and the width of the sill beneath the eastern limb (the eastern melt sill) is up to $\sim 4 \text{ km}$. Such large widths are unusual along the East Pacific Rise. Kent et al. [2000] interpret the wide eastern melt sill as evidence for enhanced melt supply at the ridge discontinuity, which is consistent with the model of continuous along-axis magma supply across the OSC at subcrustal levels [Dunn et al., 2001]. Although some geophysical studies suggest that the magma supply to the OSC may involve some significant

along-axis components [e.g., *Barth and Mutter*, 1996], these investigations nevertheless show that the OSC has a high magmatic budget at crustal levels.

[5] The Anatomy of a Ridge Axis Discontinuity (ARAD) experiment [*Singh et al.*, 1999], which was conducted in 1997 on board R/V *Maurice Ewing*, provided a large volume of refraction and reflection seismic data across the 9°03'N OSC: *Kent et al.* [2000] propose a melt supply mechanism at the OSC by presenting images of interpreted melt runnels in the vicinity of the eastern melt sill. By correlating seismic velocity images and results from magnetic analysis, *Bazin et al.* [2001] interpret the region of thick layer 2A at the tip of the propagating spreading limb and beneath the overlap basin as the result of a long period of extrusive accumulation. *Tong et al.* [2002] study the geometry of the asymmetric melt sills and vertical sections from a seismic velocity model and propose a possible self-decapitation model of the neovolcanic axis that may explain the morphologic evolution of the propagating eastern limb.

[6] Despite the previous studies of the OSC, our understanding of the upper crustal structures and processes at this ridge discontinuity is limited. First, there is little understanding of the crustal processes leading to the formation of a ridge crest with a relatively large cross-sectional area of the propagating limb, similar to that found in midsegments, as the ridge discontinuity migrates. Second, although the western melt sill has been imaged beneath the eastern part of the bathymetric ridge crest [e.g., *Tong et al.*, 2002], the relationship is unclear between the melt sill and the upper crustal structure of the retreating limb. This study complements the previous investigations by seeking to understand the apparent contradicting relationship between enhanced magma supply at crustal levels and the deep bathymetry of major ridge discontinuities, which is related to the long-debated validity of the magma supply model. We attempt to resolve the paradox by proposing a new geologic model that addresses the role of enhanced magmatism on upper crustal structures and processes in ridge discontinuity migration. We also present the details of seismic tomography, including model resolution assessment and velocity gradient and velocity anomaly models.

3. Data Processing and Analysis

3.1. Seismic Data

[7] The ARAD experiment involved firing two sets of air gun shots: the first regional set with more than 2000 shots covered the OSC and its flanks, and the second set with more than 160,000 densely spaced shots targeted more closely the overlapping parts of the ridge segments. This study uses the seismic refraction data from the second set of shots, which were fired along 201 profiles with line spacings of 100 m and shot spacing of ~38 m (Figures 1a and 1b). We used hydrophone data recorded by all the functioning instruments deployed on the seafloor, which include 18 ocean-bottom hydrophones (OBHs) and an ocean-bottom seismometer (OBS). Data recording problems and recovery failure affected all the other instruments.

[8] Linear time corrections were applied to correct for the clock drift of the OBHs/OBS. The locations of the Cambridge OBHs/OBS were determined by minimizing the travel time misfit between the observed direct arrivals in

the water layer and the travel times modeled by ray tracing. A grid-search method was employed to find the instrument location that yielded the smallest travel time misfit, assuming a one-dimensional (1-D) velocity profile in the water column, with an average value of 1.493 km s⁻¹ based on expendable bathythermograph data. The differences in OBHs/OBS deployment locations and relocated positions range from 50 to 400 m. On the basis of an average travel time residual of around 10 ms, the estimated accuracy of the relocated positions is 18 m. The depths of the OBHs/OBS were constrained to be above the local swath bathymetry, and the relocated depths of the OBHs/OBS are 0–20 m above the local bathymetry. This small misfit is consistent with the suspension of hydrophones above the seafloor (~10 m), with smoothing applied to the swath bathymetry data and pick uncertainties of the direct arrivals in the water layer. The Scripps OBHs were relocated by minimizing the travel time misfit of direct arrivals and by modeling the wave velocity in the water layer with an estimated accuracy of 5 m in the horizontal relocated position [*Bazin et al.*, 2001]. The smaller uncertainties for the Scripps OBHs are due to differences in relocation procedures and higher sampling frequency of the OBHs (4 ms rather than 7.8 ms).

[9] Data quality of the functioning OBHs/OBS is generally good, and continuous crustal arrivals are observed clearly on seismic record sections (Figure 2). The densely fired shots generally result in coherent arrivals on the record sections, which can be exploited in identifying and picking arrivals. However, due to the short interval between consecutive shots (~16 s), the resonating water column caused by the prior shot created a relatively noisy environment. As a result, only crustal arrivals with maximum source-receiver offsets of ~11 km could be identified with confidence. In this study, first crustal arrivals were picked at the first zero crossing of the signals using a semiautomatic picker in “ProMAX” (seismic software package by “Advance Geophysical Corporation”). Noisier data were picked manually. Uncertainties ranging from 12 to 82 ms were assigned to 69,786 travel time picks from 19 OBHs/OBS upon inspection. Figure 3 shows the distribution of pick uncertainties. The average pick uncertainty is 28 ms. Larger uncertainties were assigned to the noisier data with emergent or non-impulsive waveforms, usually coinciding with crustal arrivals characterized by smaller amplitudes recorded at larger source-receiver offsets or signals with more variable waveforms caused by scattering related to the rugged seafloor bathymetry. Uncertainty in instrument location and the sampling rates of the OBHs/OBS were considered when estimating the minimum pick uncertainty of 12 ms. The generally small pick uncertainties are important for determining the subtle upper crustal structure variations as the travel times are relatively small compared with those corresponding to rays that have penetrated into the lower crust. Compared with *Bazin et al.* [2001], we use substantially more travel time picks in a smaller study area.

3.2. Tomographic Method

[10] We applied an iterative tomographic inversion code “Jive3D” [*Hobro et al.*, 2003] to construct a *P* wave seismic velocity model from the travel time picks. The analysis is independent of the one presented by *Bazin et al.* [2001]. The basic method of Jive3D is to find a layer-

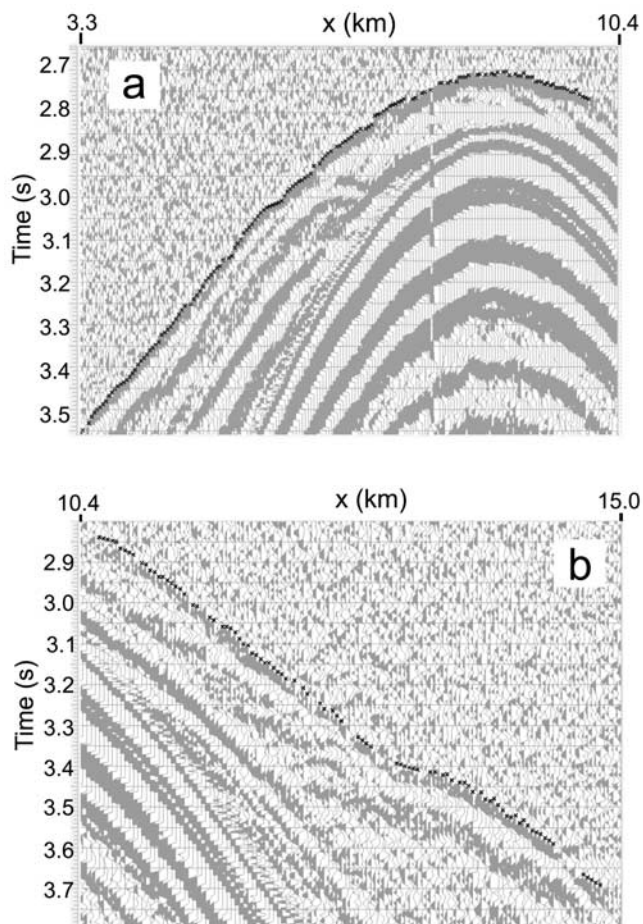


Figure 2. Two representative record sections with travel time picks (black crosses) used in the tomographic modeling. The horizontal axis is the x axis as defined in Figure 1. Note the high coherency of the crustal arrivals, partly as a result of dense shot spacing of ~ 38 m. Uncertainties of 18 and 28 ms were assigned to the picks in Figures 2a and 2b, respectively.

interface model with minimum structure by jointly minimizing travel time misfits and model roughness. The model roughness takes the form of the spatial curvature of the seismic velocity field. The travel time misfit is the difference between the travel time pick and the synthetic travel time calculated by the two-point-ray-tracing forward modeling algorithm. The inversion procedure is linearized and iterative. Velocity perturbation is calculated using the conjugate gradient method after each forward modeling step, and the perturbation is imposed on the original velocity field to produce the updated model. The advantage of this method is that velocity models are updated with small changes in ray distribution and that convergence to a solution can be readily achieved.

[11] A discrete model was constructed to represent the velocity field of the upper crust at the OSC, which is interpolated by using the B-Spline function to give velocity values between the velocity nodes. The model consists of two layers: the crustal layer and the water layer. The water layer is kept fixed with a velocity of 1.493 km s^{-1} . A relatively dense parameterization of 59×55 horizontal

nodes in an area of $29 \text{ km} \times 26.7 \text{ km}$ and 22 vertical nodes from 2.4 to 6.5 km below the sea level (71,390 nodes in total) is used to represent the crustal layer. This parameterization results in a horizontal node spacing of $500 \text{ m} \times 494 \text{ m}$ and a vertical node spacing of 195 m. The horizontal node spacing is chosen such that it is finer than the laterally resolvable structures. The crustal layer of the starting model has a velocity of 3.5 km s^{-1} at 3.4 km below the sea surface (Figure 4b, top left) with a constant velocity gradient of 1.3 s^{-1} and no horizontal variations. The two layers are separated by an interface representing the seafloor, which is based on the swath bathymetry gridded at 100 m horizontal intervals. Given that the study area has a complex bathymetry and lies at a ridge discontinuity, highly variable upper crustal structures may be expected. Therefore no specific preexisting crustal layering model was used to build the starting velocity model.

[12] The two-point-ray-tracing method calculates travel times by first finding the ray paths joining the points in the model that represent the OBHs/OBS positions and the air gun shot locations. However, due to the rugged bathymetry of the study area, some of the rays to the shot points cannot be traced, resulting in a “hit rate” of $<100\%$. However, a high proportion of rays could be traced by the algorithm (around 83%), and shots from which rays cannot be traced tend to be randomly distributed in location. (See section 4.1 for discussion on the distribution of the successfully traced rays in the preferred velocity model.)

[13] The main user-controlled parameter in the inversion of travel times is regularization, a weighting factor that controls the degree of model roughness of the new velocity model. We gradually decreased the level of regularization as the inversion progressed, and we observed a corresponding decrease in χ^2 misfit (Figure 4a). A significant decrease in χ^2 misfit is noted after the first iteration (66.1 decreasing to 3.4), and the updated velocity model shows a roughly 1-D velocity depth profile with near-constant velocity gradient (Figure 4b, top right). The misfit continues to show a decreasing trend as the level of regularization decreases, and it reaches 2.5 at the fifth iteration. The corresponding velocity model shows a two-layer structure: an upper higher-velocity gradient layer above a deeper lower velocity gradient layer (Figure 4b, bottom left). The final preferred velocity model is obtained at the twelfth iteration with a χ^2 misfit of 0.996 (Figure 4b, bottom right), which indicates

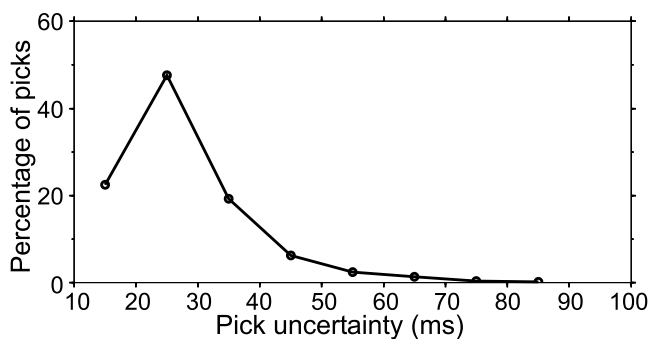


Figure 3. Distribution of the travel time pick uncertainties. A total of 69,786 ($\sim 90\%$) first arrival crustal picks were assigned uncertainties of <40 ms.

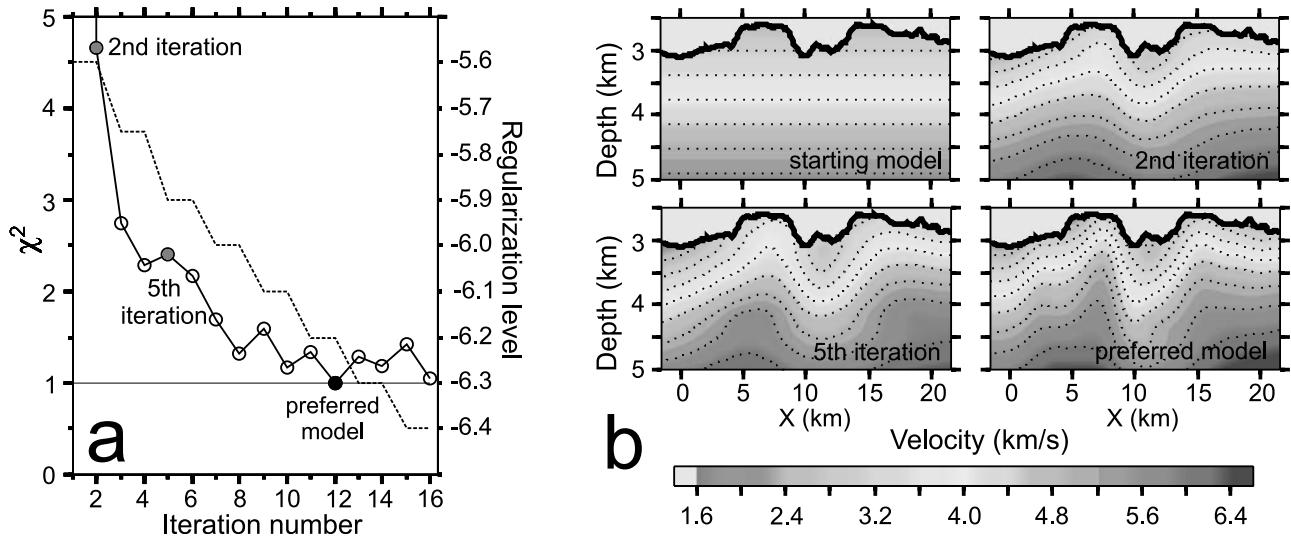


Figure 4. (a) Travel time misfit (χ^2) variation and regularization level as a function of iteration in the tomographic inversion. Black line indicates χ^2 variation, with $\chi^2 = 66.1$ after the first iteration using the starting model in Figure 4b (top left). As the regularization level (dashed line) decreases, a general decreasing trend in χ^2 is observed. Figure 4b (top right and bottom left) shows two intermediate velocity models with the corresponding χ^2 indicated in Figure 4a. The final “preferred” velocity model (Figure 4b, bottom right) is obtained after 12 iterations with $\chi^2 = 0.996$. No corresponding decrease in χ^2 is observed with further decrease in regularization level. Note that the Figure 4b models correspond to the same vertical slice of the velocity model at $y = 10$ km. See text for discussion. See color version of this figure in the HTML.

that the average travel time misfit is close to the assigned uncertainties of the travel time picks. The velocity model shows some refinements of the two-layer structure over that observed in Figure 4b (bottom left). The regularization level was allowed to decrease beyond the twelfth iteration, but no corresponding further decrease in the χ^2 misfit was observed. This result implies that the best fitting velocity model may have been obtained. The relaxation in regularization beyond the twelfth iteration does not produce a rougher velocity model that contains structure permitting further decrease in travel time misfits.

3.3. Velocity Gradient and Velocity Anomaly Models

[14] The velocity model from tomographic inversion is the primary result of this study, from which the velocity gradient and velocity anomaly models were derived. Structures can be highlighted by extracting the vertical-velocity gradient variation and comparing the local velocity with reference to the mean 1-D velocity depth profile. Vertical variation in the velocity gradient is useful in defining seismic layers. The 3-D coverage of the study area not only provides information on the variation of the thickness of seismic layers but also on the velocity gradient variation within them. Velocity anomaly models are best for illustrating structural differences between the tectonically contrasting overlapping spreading limbs.

[15] The velocity gradient is calculated at each node in the velocity model by first finding the difference in seismic velocities between vertically adjacent velocity nodes and then dividing the difference by the node spacing. The velocity anomaly model is derived by first finding the deviation in velocity from the average velocity at the depth below the local bathymetry for each node in

the velocity model. Smoothing was then applied to the model by means of a circular filter with a radius of 5 km operating on velocity nodes at the same depth below the bathymetry. A radius of 5 km was chosen to reflect the estimated resolution of the velocity model, and its precise value has insignificant effect on the resulting model. The velocity at a given velocity node has a weighting of 1, decreasing linearly to 0 at the circumference of the region within which the filter operates. Unlike the velocity gradient model, smoothing is necessary as artifacts are produced by the difference in resolution between the rugged bathymetry (100 m) and the smooth velocity field (2.5–5.0 km: refer to section 4.2).

4. Model Assessment and Modeling Results

4.1. Model Assessment

[16] Although the χ^2 misfit provides a general indication of the quality of the velocity model, it is necessary to examine the data fits and model quality in greater detail. The tomographic inversion assumes that assigned uncertainties of the travel time data follow a Gaussian distribution. It is expected that the travel time residuals of the preferred velocity model also follow a Gaussian distribution. Figure 5 shows the travel time residuals as a function of source-receiver offset. The RMS residual is 27.8 ms. Figure 5a shows the normalized residuals, which are defined as the residuals divided by the corresponding pick uncertainties. Three distributions of normalized residuals with different ranges of source-receiver offsets (each with similar numbers of residuals) show close resemblance to Gaussian distributions and thus demonstrate that the data fit is good irrespective of source-receiver offsets. The statistical aver-

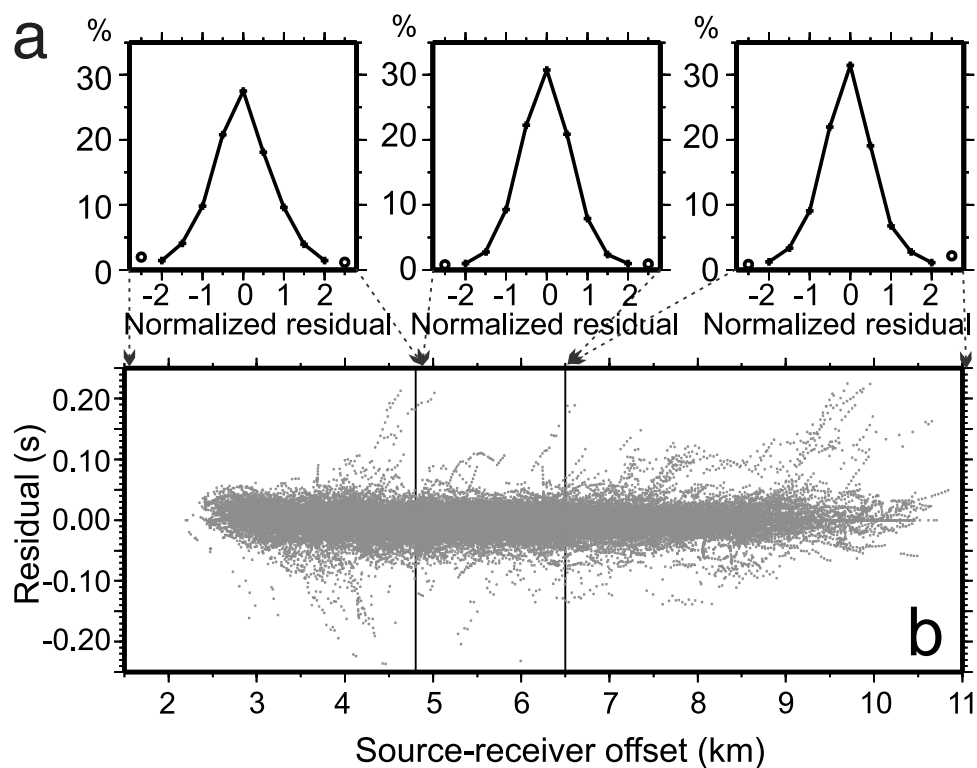


Figure 5. (a) Normalized residual distributions of the preferred velocity model are shown as the percentage of all modeled travel times in the following source-receiver offset bins: (left) 2–4.8 km; (middle) 4.8–6.5 km; and (right) 6.5–11 km. Normalized residuals are defined as the residuals divided by the corresponding pick uncertainties. The three bins contain similar numbers of picks. Percentages for the normalized residuals >2 and <-2 are indicated by circles. (b) Travel time residuals (not normalized) of the preferred velocity model as a function of source-receiver offsets.

age of all the normalized residuals is equivalent to χ^2 (0.996).

[17] The derivative weight sum (DWS) [e.g., *Toomey et al.*, 1994] is used to assess the ray distribution in the velocity model. The DWS of each velocity node is defined as the summation of all partial derivatives that correspond to the velocity node in the Fréchet derivative matrix. This value depends not only on the number of rays influencing the velocity of a particular node but also on the distance between the rays and the node. The DWS is therefore a more sophisticated measure of ray count. The distribution of DWS is important not only because rays are the sampling tool in tomography but also due to their potentially large spatial variation. The latter is influenced by experimental configuration, velocity gradient, and the inability to find rays for some source and receiver pairs in the two-point-ray-tracing algorithm of the modeling code.

[18] Checkerboard tests provide information on the lateral resolution of a velocity model by examining the ability to recover the velocity anomaly pattern superimposed on the velocity model based on a given ray distribution [e.g., *Zelt*, 1999]. We performed a checkerboard test by first superimposing a 2-D sinusoidal percentage velocity anomaly on all velocity nodes in the crustal layer of the preferred velocity model (Figure 6). The sinusoidal function has a half-wavelength of 5 km and a peak of 10% of the local velocity. Synthetic travel times are obtained by forward modeling using the perturbed

velocity model. Inversion of these synthetic travel times with uncertainties identical to those in the original inversion was then performed. The preferred velocity model (unperturbed model) was used as the starting model. The

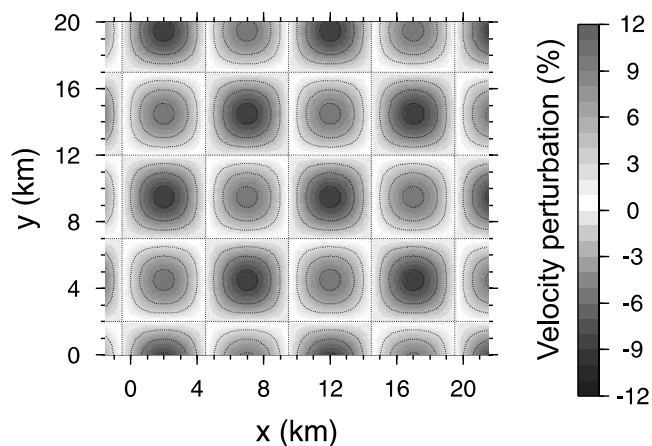


Figure 6. Percentage velocity perturbation imposed on the preferred velocity model used in the checkerboard test. The perturbation consists of a 2-D sinusoidal pattern with an amplitude of 10% of the local velocity and a half-wavelength of 5 km. See color version of this figure in the HTML.

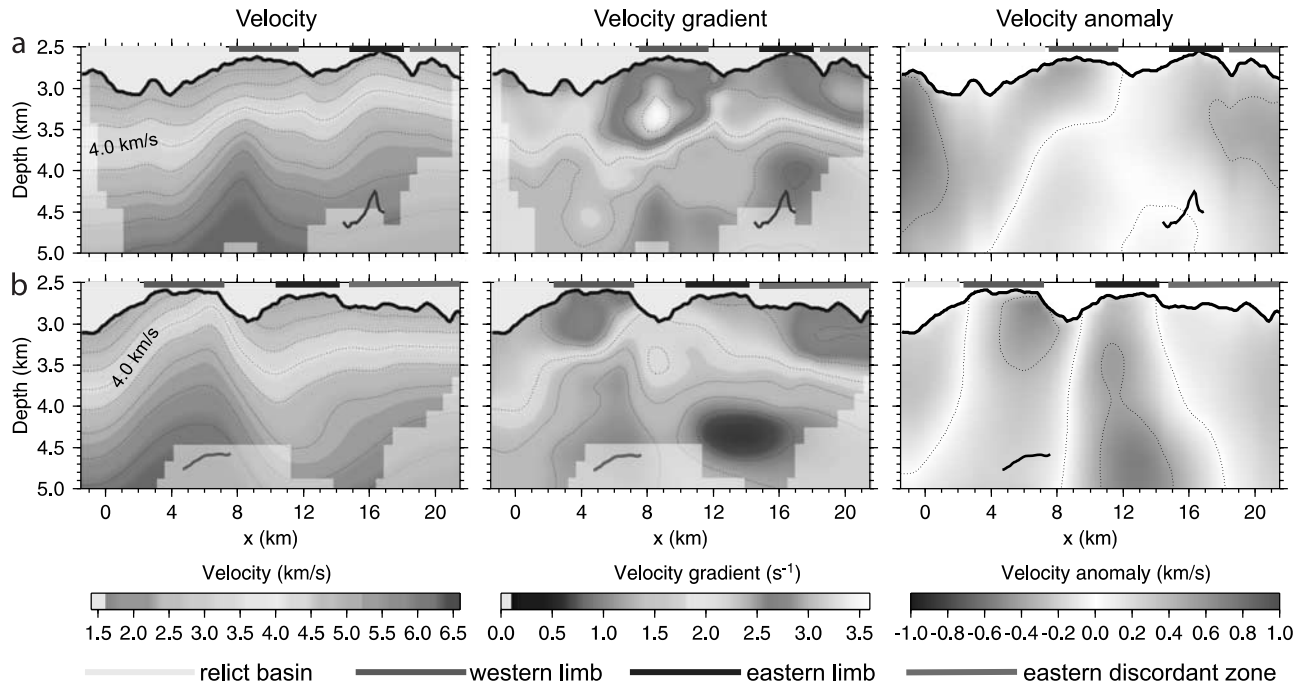


Figure 7. (a and b) (left) Vertical slices of the velocity model; (middle) velocity gradient; and (right) velocity anomaly models that correspond to line A (Figure 7a) and line B (Figure 7b) shown in Figure 1. Thick black lines show the locations of the melt sills. Regions not constrained by rays are shown in lighter shades. The 4.0 km s^{-1} contours, which are used to represent the layer 2A–2B boundary (section 5.1), are shown. See text for discussion. See color version of this figure in the HTML.

resulting velocity model from this inversion is compared with the perturbed model. A good recovery of the velocity perturbation indicates good resolution.

4.2. Velocity Models

[19] The velocity, velocity gradient, and velocity anomaly models show significant 3-D variations across the morphologic regions in the study area. Here we show two vertical sections in the northern and southern parts of the OSC (Figure 7; refer to Figure 2 of *Tong et al.* [2002] for other vertical sections) and slices at constant depths below seafloor (Figure 8) to illustrate the close relationship between the melt sills and the thickness and velocity gradient structures that characterize seismic layers 2A and 2B in the vicinity of the melt sills.

[20] A high-velocity gradient layer is observed under the western limb, which shows little structural relationship with the adjacent overlap basin and relict basins (Figures 7a and 7b, middle). The tip region of the western limb is characterized by a shallow, thick, high-velocity gradient layer (Figure 7a, middle), whereas a relatively thin high-velocity gradient layer is observed away from the tip (Figure 7b, middle). A region with low-velocity gradient is imaged at the tip of the eastern ridge tip (Figure 7b, middle). There is a gradual transition of seismic structure from the overlap basin/inter-ridge-crest area to the eastern discordant zone (Figures 7a and 7b, middle): velocity gradients in the upper layer gradually increase from the western part to the eastern part. An unusually low-velocity gradient of $\sim 0.3 \text{ s}^{-1}$ is found beneath the high-velocity gradient layer at the bathymetric ridge tip (Figure 7b, middle).

[21] The velocity at depths immediately below the seafloor is very low (about 2.5 km s^{-1}) in the tip region of the western limb (Figure 8, P1). By contrast, there is a positive velocity anomaly region at similar depths above areas where a melt sill is found (Figure 8, P3). The deeper region above the western melt sill (Figure 8, S2) has low-velocity gradients that are not observed under the bathymetric ridge tip. The velocity is higher in the eastern discordant zone (Figure 8, P3, Q3), which is in contrast to the negative velocity anomaly observed in the relict basin in the western part of the study area. A shallow low-velocity region extends from the eastern ridge tip to the overlap basin (Figure 8, Q1, R1). This area is also revealed as a region with negative velocity anomaly with low-velocity gradients, which is also a characteristic of the seismic structure under the relict basins (Figure 8, P3–S3).

[22] The variation of normalized DWS in the velocity model is shown in Figure 9, P4–S4. Our results show that there is a good correlation between the model resolution as inferred from the checkerboard test (Figure 9, P5–S5) and DWS. Model resolution is good at shallow depths. The lateral resolution of the velocity model at shallow depths (0–1.0 km below seafloor) is estimated as 2.5–5 km based on the recovery of the anomaly pattern in the checkerboard test. However, the resolution deteriorates with increasing depth. The DWS is also smaller at greater depths, indicating a broadly good correlation between the results of the two model assessment methods. Regions that are not constrained by rays (zero-normalized DWS) are masked. On the basis of the good resolution of the velocity model at shallow depths (up to 1.2 km; section 4.2), layer 2A thickness variations of greater than 195 m (vertical node

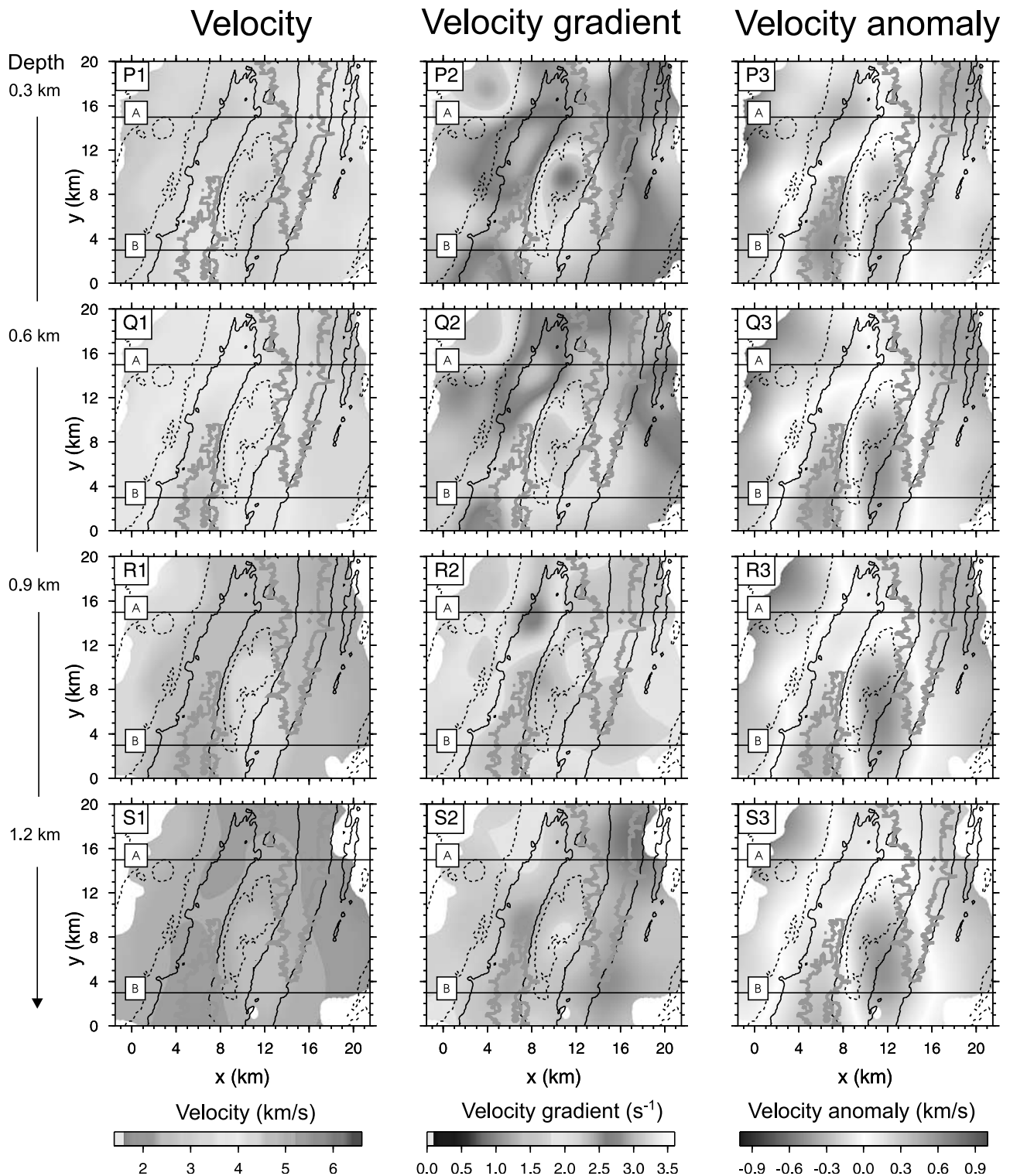


Figure 8. Slices of the velocity model (P1–S1), velocity gradient (P2–S2), and velocity anomaly models (P3–S3) at the depths of 0.3, 0.6, 0.9, and 1.2 km below seafloor. Lines A and B are shown for cross-reference with Figure 7. Solid black lines show the ridge crests of the limbs (<2700 m), and dotted lines indicate locations of the overlap basin and relict basins (>2900 m). Regions with no ray constraints are masked. The gray lines delineate the melt sills. See text for discussion. See color version of this figure in the HTML.

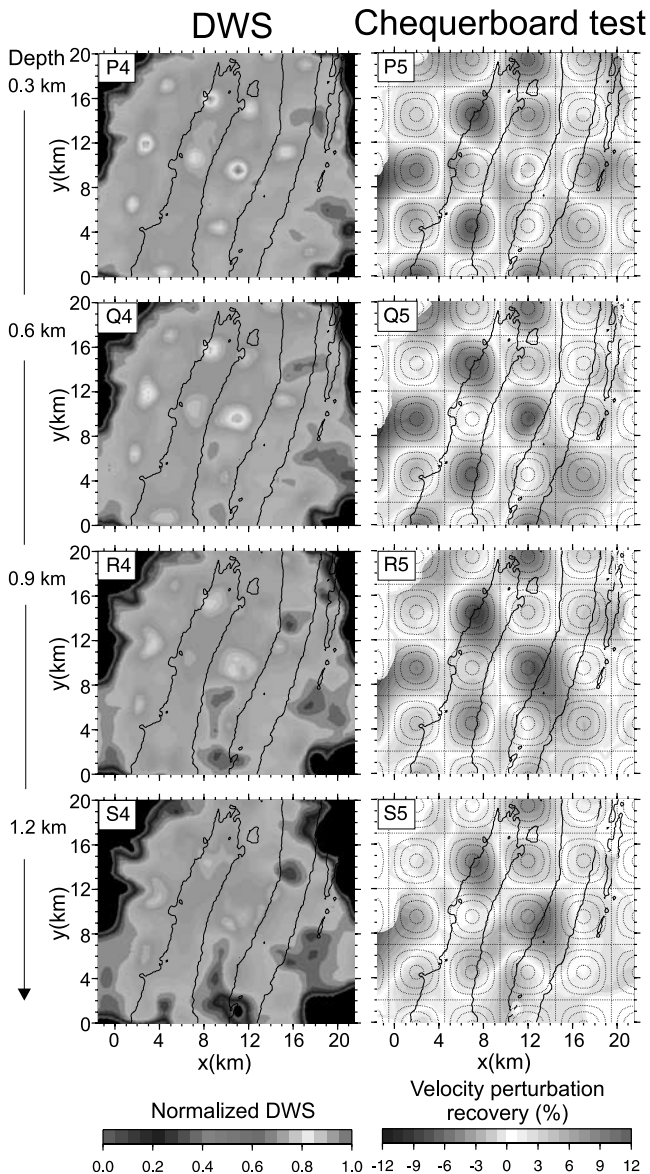


Figure 9. Variations in the normalized derivative weight sum (DWS) (P4–S4) and the recovery pattern in the checkerboard test (P5–S5) at the depths of 0.3, 0.6, 0.9, and 1.2 km below seafloor. A good recovery of the perturbation pattern is observed, indicating good model resolution at shallow depths. See text for interpretation. See color version of this figure in the HTML.

spacing) in the horizontal scale of 2.5–5.0 km can be considered to be resolved adequately.

5. Interpretation

5.1. Layer 2A–2B Boundary

[23] The subdivision of the upper oceanic crust into seismic layers 2A and 2B (layer 1 corresponds to the sediment layer) is generally based on the significant change in velocity gradient at the interface between the two seismic layers. Layer 2A is characterized by low velocities ($\sim 3.5 \text{ km s}^{-1}$) and high velocity gradients ($> 2 \text{ s}^{-1}$). The underlying layer 2B is identified as the layer with an

average velocity of $\sim 5.2 \text{ km s}^{-1}$ and lower velocity gradients ($\sim 1 \text{ s}^{-1}$). Using the velocity gradient criterion, the tomographic image from this study shows that the upper crust at the OSC similarly can be divided into layers 2A and 2B. Velocity contours of $4.0\text{--}4.5 \text{ km s}^{-1}$ generally separate the upper high-velocity gradient layer from the lower low-velocity gradient layer (Figure 7). *Bazin et al.* [2001] use the velocity contour of 4.0 km s^{-1} to represent the layer 2A–layer 2B boundary in their tomographic model of the OSC. We use the same velocity contour here to represent the boundary.

[24] In order to avoid significant artifacts caused by the large difference in lateral resolution between the rugged bathymetry and the seismic velocity field, we smooth the bathymetry to $1 \text{ km} \times 1 \text{ km}$ before subtracting it from the depth of the 4.0 km s^{-1} velocity contour to obtain the estimated thickness of layer 2A (Figure 10a). The resulting average thickness of layer 2A in the study area is 550 m, and it ranges from 210 to 940 m. Using a contour of slightly higher velocity (e.g., 4.5 km s^{-1}) would increase the thickness of layer 2A, but the variation in thickness, upon which our interpretation is based, would be minimally affected.

[25] Compared with the thickness of layer 2A observed in midsegments of ridges, a relatively thick layer 2A is imaged using the 4.0 km s^{-1} velocity contour as the working definition of the layer 2A–2B boundary. However, this result agrees with those from previous studies conducted near ridge discontinuities [*Hoofi et al.*, 1996; *Van Avendonk et al.*, 2001; *Bazin et al.*, 2001]. *Bazin et al.* [2001] reported that the layer 2A thickness in the 9°N area varies from 100 to 900 m, with an average of 430 m. Regions of thick layer 2A are imaged in the relict basins, overlap basin, and the tip region of the eastern ridge tip in both studies. Our results therefore confirm the previous results by analyzing a larger subset of seismic refraction data using a different tomographic method. Nevertheless, our interpretation and discussion of these results have not been previously reported.

5.2. Formation of Ridge Crest Morphology at the Propagating Limb

[26] In this section, we examine the upper crustal structure of the eastern ridge tip and overlap basin as well as that above the eastern melt sill away from the ridge tip. By evaluating the existing geologic models using our observations, we study the upper crustal processes related to the formation of ridge crest morphology at the propagating limb. We image an extensive region with anomalously thick layer 2A ($\sim 800 \text{ m}$ thick) at the tip of the eastern limb and the overlap basin (Figure 10) with thickness similar to that reported by *Bazin et al.* [2001]. The hummocky bathymetry of the inner flank (relative to the overlap basin) of the eastern limb tip shows signs of extrusive pileup [*Bazin et al.*, 2001], and dike propagation [*Dziak et al.*, 1995; *Embley et al.*, 2000] is likely to be the main mechanism of building the upper crust south of the melt sill. The highly asymmetric ridge crest morphology with a steep outside flank (relative to the overlap basin) as well as the lack of surficial lineations and fissures in the overlap basin provide strong support for the high levels of extrusive emplacement that may account for the region of thick layer 2A [*Bazin et al.*, 2001]. However, this thickness anomaly of layer 2A may partially be the result of high bulk porosity due to high levels of extensional stress at the tip of the eastern limb [*Tong et al.*, 2002]. The significantly lower

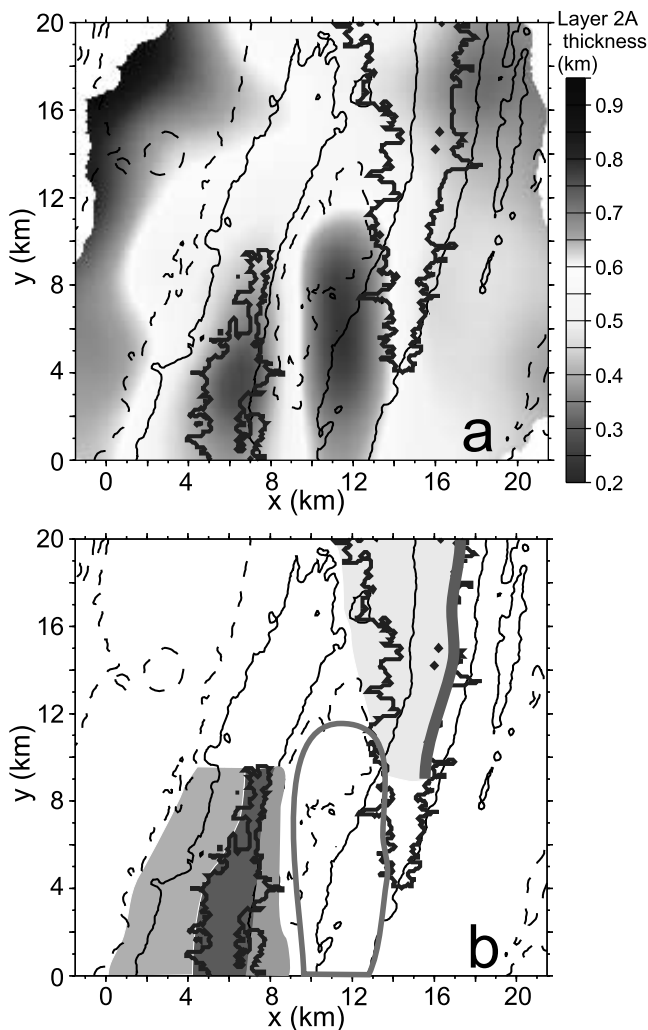


Figure 10. (a) Layer 2A thickness in the study area as inferred from the 4.0 km s^{-1} isovelocity contour. Regions not constrained by rays are masked. The geometry of the melt sills is shown by the dark blue lines. Thin layer 2A is observed above the western melt sill. Thick layer 2A is imaged beneath the overlap basin and the tip of the eastern limb, as well as the relict basins. (b) Key upper crustal features related to the melt sills. Asymmetric magmatism is associated with the thin extrusives (red region) above the western melt sill as well as the off-axis thickening extrusives to its west (green region), particularly toward the tip of the melt sill. In contrast, the region with thickening extrusives to the east of the western melt sill appears to be more limited (gray region). Thickening extrusives are inferred above the eastern melt sill (yellow region) to the west of the neovolcanic axis (thick red line). Thick extrusives, whose bulk porosity structure may be modified by extensional stress field at the ridge tip, are interpreted at the tip of the eastern limb and overlap basin (enclosed by thick blue line). See text for detailed discussion. See color version of this figure in the HTML.

velocity gradients of the thick extrusives in this region compared with those above the melt sill (Figure 8) may be related to this distinct porosity structure. Nevertheless, these two interpretations are not mutually exclusive because sig-

nificant reduction in bulk porosity may be subsurficial, which would not contradict the observation of a lack of surficial fissures. The observation that this thickness anomaly extends from the ridge tip to an extensive part of the overlap basin suggests that the seismic structure of the overlap basin is predominantly related to the propagating limb.

[27] On the basis of the bathymetric observation of a summit trough [Sempéré and Macdonald, 1986], the location of the inferred neovolcanic axis and the shallowest region of the melt sill [Tong et al., 2002], the highest level of volcanic activity appears to be found near the eastern edge of the melt sill. There is a systematic increase in the thickness of layer 2A from the neovolcanic axis ($\sim 350 \text{ m}$) to the western edge of the melt sill ($\sim 550 \text{ m}$) (Figure 10). However, no increase in layer 2A thickness to the east of the neovolcanic axis is observed. By using the lithologic interpretation of the layer 2A–2B boundary, we infer that the thickening of extrusives is mainly found above the melt sill and the interridge-crest region. This asymmetry is consistent with the model of self-decapitation of the neovolcanic axis of the propagating limb [Tong et al., 2002], which results in the discordant zone to the east of the propagating limb. Consistent with this asymmetry, fault density is significantly higher in the discordant zone than it is near the ridge crest [Carbotte and Macdonald, 1992].

[28] The ridge crest morphology of fast-spreading ridges is generally considered to be the result of the buoyancy of hot rock and magma beneath the rise but is not mainly a volcanic construction feature [e.g., Madsen et al., 1984]. However, based on the observation of relict ridge tips on the flanks of fast-spreading ridges, Carbotte and Macdonald [1994] proposed that overlapping ridges are likely to comprise a significant volcanic construction component. Our interpretations of the upper crustal structure of the eastern limb may therefore provide insights into the transition from the model of volcanic construction to the buoyancy mechanism in explaining the observed ridge crest morphology at the OSC. The significant extrusive pileup at the propagating ridge tip may represent the initial phase of volcanic construction of the ridge crest, where no melt sills have been observed. The ridge crest has a relatively small cross-sectional area and a hummocky surface. The existence of a wide melt sill away from the tip suggests that there is more hot buoyant material supporting a broader ridge crest. Although it is difficult to determine the relative contribution of reduction in bulk porosity on the thick layer 2A imaged at the eastern ridge tip ($\sim 800 \text{ m}$), the on-axis extrusives away from the tip appear to be significantly thinner ($\sim 350 \text{ m}$). The contribution from volcanic construction for the formation of a ridge crest with a larger cross-sectional area is likely to decrease with distance away from the propagating tip resulting in a thinner extrusive layer, whereas the buoyancy factor becomes more dominant. This region signifies the second phase of ridge crest formation. These main stages support the model of the southward advancement of the melt sill with the propagating limb [Tong et al., 2002].

5.3. Asymmetric Extrusive Emplacement Geometry of the Western Limb

[29] The good match in the locations of the positive velocity anomalies and the western melt sill suggests that the melt sill has a direct influence on the upper crustal

construction of the western limb (Figure 8, P3–S3). Although layer 2A is on average thicker in the study area than along midsegments, the thin layer 2A above the western melt sill, which results in the positive velocity anomalies, is similar to the typical on-axis seismic structure observed elsewhere on the East Pacific Rise [e.g., *Harding et al.*, 1993]. On the basis of the lithologic interpretation of layer 2A as extrusive volcanics [e.g., *Harding et al.*, 1993; *Christeson et al.*, 1994], our results indicate that the on-axis extrusive layer at the magmatically weaker western limb is thin (~250 m) and exhibits little variation in thickness above the melt sill (Figure 10a).

[30] The most prominent across-axis variation in layer 2A thickness in the western limb is the asymmetric geometry of thickening of the seismic layer to the west of the melt sill (from ~200 to ~550 m). A high-velocity gradient region is also imaged in the same area (Figure 8, P2 and Q2), but not to the east of the melt sill. The asymmetry is closely related to the eastward displacement of the melt sill relative to the ridge crest and the seismic structure of the overlap basin, which is predominantly influenced by the propagating limb (section 5.2, Figure 10). Also, this asymmetry is particularly pronounced toward the tip of the melt sill. We interpret this asymmetric thickening of layer 2A with a corresponding region of high velocity gradients as the result of the asymmetric extrusive emplacement of the western limb. Morphologically, this interpretation is supported by the gentler slope of the outer flank of the ridge crest than that of the inner one (Figures 1 and 10; Figure 3a of *Sempéré and Macdonald* [1986]), which may be related to the surficial overflow of lava on the outer flank. This model is supported by the observed transition in the characteristics of the seafloor from the magmatically active southern part to the northern part, where little recent volcanic activity has been reported and more faults and fissures have been observed [*Sempéré and Macdonald*, 1986].

[31] The horizontal scale of layer 2A thickening (up to ~4 km to the west of the melt sill in an along-axis region of 8 km; Figure 10) and the degree of thickening (from ~200 to ~550 m) are compatible with those reported in previous studies [e.g., *Vera et al.*, 1990; *Toomey et al.*, 1990, 1994; *Harding et al.*, 1993]. In contrast, the thickening of extrusives to the east of the melt sill appears to be restricted to a narrower region (1.0–1.5 km) based on the steep inner flank morphology. We prefer the lithologic interpretation of the thickening of layer 2A to the model of changes in bulk porosity for explaining our observation: the outer flank of the ridge crest away from the ridge tip is less likely to be subject to major porosity changes caused by the high stress field associated with the interaction between the overlapping cracks.

[32] We propose that this newly observed asymmetric extrusive accumulation geometry appears to be related to the various stages of self-decapitation. Although self-decapitation of ridge segments is generally associated with a decline in magmatic activity [*Macdonald et al.*, 1987], our inference of construction of the upper crust on the outer flank of the western limb suggests that this asymmetric magmatism of the western melt sill may be related to this anticlockwise motion of the western limb. As the melt sill geometry is controlled by the deeper, ductile

behavior of the plate boundary [*Tong et al.*, 2002], the relative anticlockwise motion of the western limb with respect to the melt sill would in the long term result in a wider region of extrusive emplacement to the west of the melt sill. It is interesting to compare our observations with the presence of high volcanic activity of the failing rift in some propagating rift systems [*Macdonald*, 1989]. However, it appears that such a contribution of asymmetric extrusive emplacement will decrease with time as the melt sill continues to retreat. The decline of magmatism at the tip region of the western limb [e.g., *Sempéré and Macdonald*, 1986] will migrate to the south. The eventual disappearance of the melt sill beneath the dying limb may mark the onset of the decapitation of the western limb.

6. Discussion: Along-Axis Pattern of Magmatic Budget and Ridge Crest Formation at Ridge Discontinuities

[33] The variations in cross-sectional area and bathymetry of the ridge crest as well as the spatial distribution of the axial summit graben and hydrothermal activity along mid-ocean ridge segments have been correlated with various indicators of magma supply, the most obvious of which is the geometry of the melt sills [e.g., *Macdonald and Fox*, 1988; *Scheirer and Macdonald*, 1993]. The magma supply model is used to explain these along-axis morphologic variations by attributing them to the varying levels of magmatic budget along ridge segments: the more inflated midsegments experience higher levels of magma supply than do the ridge segment ends. Hence the general validity of the magma supply model is called into question by the observation of wide melt sills [*Collier and Sinha*, 1992; *Kent et al.*, 2000; *Tong et al.*, 2002] or by the model of continuous subcrustal magma supply [*Dunn et al.*, 2001] at some major ridge discontinuities. These studies provide counterexamples that may contradict the magma supply model. However, the paradox between high levels of melt availability within the crust and relatively deep bathymetric ridge crests remains enigmatic.

[34] Despite the ridge crests with relatively small cross-sectional area, our results demonstrate that there is significant volcanic construction in both limbs of the OSC. As discussed in section 5.2, the formation of ridge crest morphology at OSCs with a significant component of volcanic construction is consistent with the observation of relict ridges on the flanks of the ridge axis [*Carbotte and Macdonald*, 1994]. Although the magma supply model attempts to explain the general bathymetric variations along the ridge axis as a function of the level of magma supply, the availability of melt required by the evolution of the ridge axis by mechanisms such as ridge propagation has not been considered. The apparent contradiction between the high magmatic budget inferred from recent seismic studies at OSCs and the magma supply model can thus be resolved by considering the rapidly evolving ridge crest configuration. The enhanced magma supply at crustal levels is consumed in ridge propagation and the related ridge crest formation processes as well as the magmatically active process of self-decapitation of the western limb by the long-term asymmetric geometry of extrusive emplacement inferred in this study (section 5.3). As a

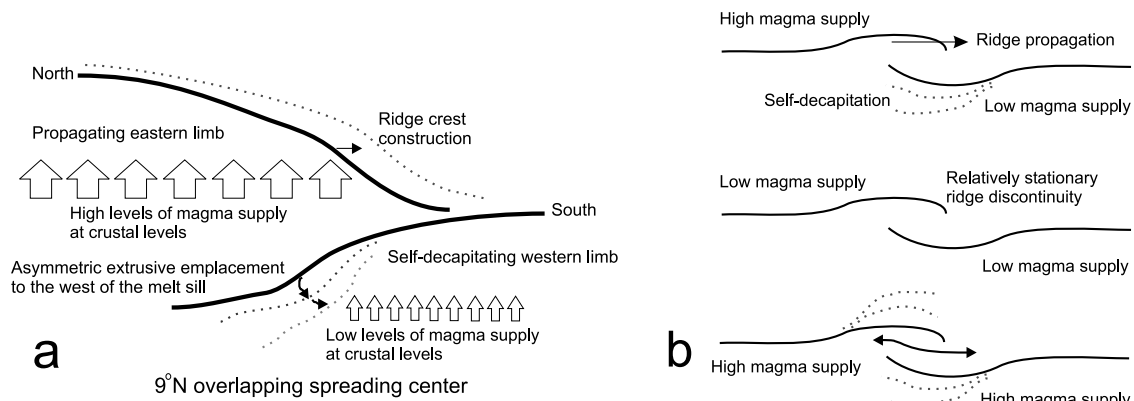


Figure 11. (a) A schematic diagram showing the relationship between the enhanced magma supply at crustal levels and ridge crest construction processes of the OSC in this study. The high levels of magma supply to the eastern limb at crustal levels is consumed in ridge crest construction processes related to ridge propagation at the OSC, and the lower levels of magma supply to the western limb is associated with the asymmetric magmatism in the self-decapitating limb. (b) The levels of magma supply to the spreading limbs of the overlapping spreading centers at crustal levels may determine the evolution of the ridge discontinuity. Ridge propagation and ridge discontinuity migration may be the result of different levels of magma supply to the spreading limbs within the crust (Figure 11b, top). Dotted lines show abandoned ridge segments as a result of self-decapitation. A relatively stationary overlapping spreading center may be the result of low levels of magma supply to both limbs (Figure 11b, middle). High levels of magma supply to the entire overlapping spreading center within the crust may generate a new ridge segment (double-angled line in Figure 11b, bottom), which is consistent with the model proposed by *Cormier et al.* [1996]. Self-decapitation of both limbs may be observed. Enhanced magma supply to major ridge discontinuities is essential for ridge crest building processes in both spreading limbs in Figure 11b (top and bottom). This “dynamic magma supply model” may explain the range of migration rate and direction of ridge discontinuities observed. Temporal changes in magma supply to the limbs of an overlapping spreading center within the crust may explain the nonsteady migratory behavior of the ridge discontinuity.

result, migrating ridge discontinuities may still be characterized by deep bathymetry despite robust magmatism.

[35] The significant levels of magmatism at the OSC may also have implications for understanding the role of melt supply in the mechanism of ridge discontinuity migration. Fracture mechanics and a model of the release of gravitational potential energy were used to explain ridge propagation at the Galapagos propagating rift [*Phipps Morgan and Parmentier*, 1985; *Parmentier and Schubert*, 1989]. However, the difference in bathymetry between the propagating and retreating segments on the East Pacific Rise does not appear to be sufficient to drive the propagation [*Cormier et al.*, 1996]. By treating ridge segments as propagating cracks, *Macdonald et al.* [1991] study the influence of far-field and near-field stresses and conclude that longer ridge segments tend to lengthen at the expense of the shorter ones. However, the crack propagation model, without resorting to a significant contribution from magmatism, may not easily explain the commonly observed dueling propagation, in which ridge segments alternately lengthen and shorten [*Carbotte and Macdonald*, 1992; *Korenaga and Hey*, 1996].

[36] We propose a “dynamic magma supply model” in which the temporal fluctuations in melt availability at crustal levels at OSCs and the contrast in magmatic budget in the adjacent ridge segments would affect the migration direction of a ridge discontinuity. The temporal fluctuations in melt availability may, for instance, be related to the

various stages of the tectono-magmatic cycle. The enhanced magmatism may be essential in ridge propagation and self-decapitation, ridge crest formation and reorientation processes active at highly evolving ridge discontinuities (Figures 11a and 11b, top).

[37] The propagating limb would have a greater magmatic budget (Figure 11b, top). *Carbotte and Macdonald* [1992] estimate that the 9°03'N OSC has migrated at an average rate of 42 mm yr⁻¹ since anomaly 2 time. This high migration rate, which is ~30% of the full spreading rate of the ridge segment, implies that a significant amount of magma is turned into the propagating ridge crest at the OSC. The unusually wide eastern melt sill, and the extensive region of pillow lava and volcanic edifices at the eastern ridge tip and the overlap basin [*Sempéré and Macdonald*, 1986] suggest high levels of magmatism at the propagating limb. The increase in crustal thickness toward the OSC from the north [*Barth and Mutter*, 1996] and the significant increase in the width of the melt sill south of the 9°17'N deval [*Kent et al.*, 1993b] may suggest that the high level of magmatism of the eastern limb and the ridge segment to its north plays an important role in ridge propagation. Dependent on the thermal structure, the crust of the propagating limb may be thicker than that of the western limb [*Barth and Mutter*, 1996], indicating that there may be a higher magma supply at the propagating limb. An alternative view to enhanced magma supply at subcrustal levels at the OSC also suggests that the propagating limb is likely to experience high levels

of melt availability at crustal levels: although the OSC may not have an increased melt supply locally from the mantle, high levels of melt availability at the propagating limb can be obtained from inferred along-axis melt migration [Barth, 1994]. Petrologic studies [e.g., Langmuir et al., 1986] and the Moho geometry at the OSC suggest that the propagating limb may have obtained the melt source from the western limb at crustal levels [Barth, 1994]. The high magmatic budget of the propagating limb is also evident from the anomalously wide lower crustal partial melt zone beneath the eastern limb and the interridge-crest region to the north of the overlap basin [Crawford and Webb, 2002]. In contrast, the lower magmatic budget of the western limb results in the self-decapitation and the declining magmatism in the vicinity of the western melt sill. The lack of recent magmatism at the ridge tip [Sempéré and Macdonald, 1986], the significantly smaller western melt sill, and the possibly thinner crust at the western limb [Barth and Mutter, 1996] suggest that there is less melt available at crustal levels at the western limb.

[38] Since not all OSCs are rapidly migrating ridge discontinuities [Macdonald et al., 1991], we speculate that only highly evolving OSCs experience enhanced magma supply at crustal levels. A relatively stationary ridge discontinuity may be the result of low levels of magma supply to both spreading limbs at crustal levels (Figure 11b, middle). However, if both spreading limbs and the ridge discontinuity experience high levels of magma supply, new ridge segment may be generated (Figure 11b, bottom). This scenario is similar to the model of bisection of overlapping spreading centers associated with robust magma supply [Cormier et al., 1996]. According to this model, self-decapitation of both limbs may also occur. The levels of magma supply to the overlapping spreading limbs may therefore explain the observed range of migration rates and directions of overlapping spreading centers [e.g., Cormier et al., 1996; Korenaga and Hey, 1996]. The temporally varying levels of magma supply to the overlapping limbs at crustal levels may explain the ubiquitous changes in propagation direction and migration rate of a single ridge discontinuity, including the 9°03'N OSC [e.g., Carbotte and Macdonald, 1992; Korenaga and Hey, 1996]. It is important to emphasize that this dynamic magma supply model may have implications but does not depend on the pattern of along-axis melt migration. The model merely links the pattern of local magmatic budget to the evolutionary aspects of the ridge axis.

7. Conclusions

[39] On the basis of our 3-D seismic tomographic model of the 9°03'N OSC, we conclude that there are significant levels of volcanic construction at the ridge discontinuity. The propagating limb is likely to acquire its ridge crest morphology with a relatively large cross-sectional area similar to that found in the midsegment by a significant component of volcanic construction, especially in the tip region. This contribution from volcanic construction is likely to decrease as the melt sill is formed. The observed asymmetric extrusive emplacement geometry, which is associated with the relative anticlockwise rotation of the

western limb with respect to the western melt sill, demonstrates that magmatism may play an important part in the evolution of the dying limb. We predict that the eventual retreat of the melt sill from the western limb and hence magmatic activities may mark the onset of the cutoff of the western limb from the main ridge axis.

[40] The apparent contradiction between the magma supply model and enhanced magmatism at OSCs may be resolved by our proposed dynamic magma supply model. Using the results and interpretations in this study, we propose that enhanced magmatism is required in a region where a highly evolving ridge crest configuration is observed. The temporally varying and contrasting levels of magma supply to the two limbs at crustal levels may determine the direction and rate of OSC migration. The model may also explain the range of migration rates and directions of ridge discontinuities observed at fast and intermediate-spreading rate ridges. The magma supply model [e.g., Sempéré and Macdonald, 1986] provides a general framework for correlating magmatic and tectonic segmentations, whereas the temporal variations in the levels of melt availability at crustal levels, especially at ridge discontinuities, may influence the evolution of the pattern of tectonic segmentation along the ridge axis.

[41] **Acknowledgments.** We thank D. Boschi, P. Henkart, C. Hollinshead, T. Owen, and P. Zimmer for work on OBHs and OBSs. The ARAD experiment was funded by the UK Natural Environment Research Council (NERC) and the National Science Foundation. C. H. T. gratefully acknowledges financial support from the NERC and Trinity College, Cambridge. P. J. B. acknowledges the support of the Newton Trust. We thank the two reviewers and the Associate Editor for their comments on the manuscript. This study was supported by Department of Earth Sciences, University of Cambridge, Contribution ES7468.

References

- Barth, G. A., Plate boundary geometry to Moho depths within the 9°03'N and 12°54'N overlapping spreading centers of the East Pacific Rise, *Earth Planet. Sci. Lett.*, *128*, 99–112, 1994.
- Barth, G. A., and J. C. Mutter, Variability in oceanic crustal thickness and structure: Multichannel seismic reflection results from the northern East Pacific Rise, *J. Geophys. Res.*, *101*, 17,951–17,975, 1996.
- Bazin, S., et al., Three-dimensional shallow crustal emplacement at the 9°03'N overlapping spreading center on the East Pacific Rise: Correlations between magnetization and tomographic images, *J. Geophys. Res.*, *106*, 16,101–16,117, 2001.
- Carbotte, S., and K. C. Macdonald, East Pacific Rise 8°–10°30'N: Evolution of ridge segments and discontinuities from SeaMARC II and three-dimensional magnetic studies, *J. Geophys. Res.*, *97*, 6959–6982, 1992.
- Carbotte, S. M., and K. C. Macdonald, The axial topographic high at intermediate and fast spreading ridges, *Earth Planet. Sci. Lett.*, *128*, 85–97, 1994.
- Carbotte, S. M., J. C. Mutter, and L. Q. Xu, Contribution of volcanism and tectonism to axial and flank morphology of the southern East Pacific Rise, 17°10'–17°40'S, from a study of layer 2A geometry, *J. Geophys. Res.*, *102*, 10,165–10,184, 1997.
- Carbotte, S. M., A. Solomon, and G. Ponce-Corra, Evaluation of morphological indicators of magma supply and segmentation from a seismic reflection study of the East Pacific Rise 15°30'–17°N, *J. Geophys. Res.*, *105*, 2737–2759, 2000.
- Carlson, R. L., Seismic velocities in the uppermost oceanic crust: Age dependence and the fate of layer 2A, *J. Geophys. Res.*, *103*, 7069–7077, 1998.
- Christeson, G. L., G. M. Purdy, and G. J. Fryer, Seismic constraints on shallow crustal emplacement processes at the fast spreading East Pacific Rise, *J. Geophys. Res.*, *99*, 17,957–17,973, 1994.
- Collier, J. S., and M. C. Sinha, Seismic mapping of a magma chamber beneath the Valu Fa Ridge, Lau Basin, *J. Geophys. Res.*, *97*, 14,031–14,053, 1992.
- Cormier, M.-H., D. S. Scheirer, and K. C. Macdonald, Evolution of the East Pacific Rise at 16°–19°S since 5 Ma: Bisection of overlapping spreading

- centers by new, rapidly propagating ridge segments, *Mar. Geophys. Res.*, **18**, 53–84, 1996.
- Crawford, W. C., and S. C. Webb, Variations in the distribution of magma in the lower crust and at the Moho beneath the East Pacific Rise at 9°–10°N, *Earth Planet. Sci. Lett.*, **203**, 117–130, 2002.
- Day, A. J., C. Pierce, and M. C. Sinha, Three-dimensional crustal structure and magma chamber geometry at the intermediate-spreading, back-arc Valu Fa Ridge, Lau Basin—Results of a wide-angle seismic tomographic inversion, *Geophys. J. Int.*, **146**, 31–52, 2001.
- Dunn, R. A., D. R. Toomey, R. S. Detrick, and W. S. D. Wilcock, Continuous mantle melt supply beneath an overlapping spreading center on the East Pacific Rise, *Science*, **291**, 1955–1958, 2001.
- Dziak, R. P., C. G. Fox, and A. E. Schreiner, The June–July-1993 seismo-acoustic event at CoAxial segment, Juan-de-Fuca Ridge: Evidence for a lateral dike injection, *Geophys. Res. Lett.*, **22**, 135–138, 1995.
- Embley, R. W., W. W. Chadwick, M. R. Perfit, M. C. Smith, and J. R. Delaney, Recent eruptions on the CoAxial segment of the Juan de Fuca Ridge: Implications for mid-ocean ridge accretion processes, *J. Geophys. Res.*, **105**, 16,501–16,525, 2000.
- Harding, A. J., G. M. Kent, and J. A. Orcutt, A multichannel seismic investigation of upper crustal structure at 9°N on the East Pacific Rise: Implications for crustal accretion, *J. Geophys. Res.*, **98**, 13,925–13,944, 1993.
- Hobro, J. W. D., S. C. Singh, and T. A. Minshull, Three-dimensional tomographic inversion of combined reflection and refraction seismic travel-time data, *Geophys. J. Int.*, **152**, 79–93, 2003.
- Hoof, E. E. E., H. Schouten, and R. S. Detrick, Constraining crustal emplacement processes from the variation in seismic layer 2A thickness at the East Pacific Rise, *Earth Planet. Sci. Lett.*, **142**, 289–309, 1996.
- Kent, G. M., A. J. Harding, and J. A. Orcutt, Distribution of magma beneath the East Pacific Rise near the 9°03'N overlapping spreading center from forward modeling of CDP data, *J. Geophys. Res.*, **98**, 13,971–13,996, 1993a.
- Kent, G. M., A. J. Harding, and J. A. Orcutt, Distribution of magma beneath the East Pacific Rise between the Clipperton transform and the 9°17'N Deval from forward modeling of CDP data, *J. Geophys. Res.*, **98**, 13,945–13,969, 1993b.
- Kent, G. M., et al., Evidence from three-dimensional seismic reflectivity images for enhanced melt supply beneath mid-ocean-ridge discontinuities, *Nature*, **406**, 614–618, 2000.
- Korenaga, J., and R. N. Hey, Recent dueling propagation history at the fastest spreading center, the East Pacific Rise, 26°–32°S, *J. Geophys. Res.*, **101**, 18,023–18,041, 1996.
- Langmuir, C. H., J. F. Bender, and R. Batiza, Petrology and tectonic segmentation of the East Pacific Rise, 5°30' to 14°30'N, *Nature*, **322**, 422–429, 1986.
- Macdonald, K. C., Mid-ocean ridges—Propagating rifts exposed, *Nature*, **342**, 740–741, 1989.
- Macdonald, K. C., and P. J. Fox, Overlapping spreading centres: New accretion geometry on the East Pacific Rise, *Nature*, **302**, 55–58, 1983.
- Macdonald, K. C., and P. J. Fox, The axial summit graben and cross-sectional shape of the East Pacific Rise as indicators of axial magma chambers and recent volcanic eruptions, *Earth Planet. Sci. Lett.*, **88**, 119–131, 1988.
- Macdonald, K. C., J. C. Sempéré, P. J. Fox, and R. Tyce, Tectonic evolution of ridge-axis discontinuities by the meeting, linking, or self-decapitation of neighboring ridge segments, *Geology*, **15**, 993–997, 1987.
- Macdonald, K. C., D. S. Scheirer, and S. M. Carbotte, Mid-ocean ridges: Discontinuities, segments and giant cracks, *Science*, **253**, 986–994, 1991.
- Madsen, J. A., D. W. Forsyth, and R. S. Detrick, A new isostatic model for the East Pacific Crest, *J. Geophys. Res.*, **89**, 9997–10,015, 1984.
- Parmentier, E. M., and G. Schubert, Rift propagation, *Geophys. Res. Lett.*, **16**, 183–186, 1989.
- Peirce, C., I. M. Turner, and M. C. Sinha, Crustal structure, accretionary processes and rift propagation: A gravity study of the intermediate-spreading Valu Fa Ridge, Lau Basin, *Geophys. J. Int.*, **146**, 53–73, 2001.
- Phipps Morgan, J., and E. M. Parmentier, Causes and rate-limiting mechanisms of ridge propagation: A fracture mechanics model, *J. Geophys. Res.*, **90**, 8603–8612, 1985.
- Scheirer, D. S., and K. C. Macdonald, Variation in cross-sectional area of the axial ridge along the East Pacific Rise: Evidence for the magmatic budget of a fast-spreading center, *J. Geophys. Res.*, **98**, 7871–7885, 1993.
- Sempéré, J. C., and K. C. Macdonald, Deep-tow studies of the overlapping spreading centers at 9°03'N on the East Pacific Rise, *Tectonics*, **5**, 881–900, 1986.
- Singh, S. C., M. C. Sinha, A. J. Harding, G. M. Kent, P. J. Barton, J. A. Orcutt, R. S. White, and R. W. Hobbs, Preliminary results from mid-ocean ridge three-dimensional seismic reflection survey, *Eos Trans. AGU*, **80**, 181, 185, 1999.
- Tolstoy, M., A. J. Harding, and J. A. Orcutt, Deepening of the axial magma chamber on the southern East Pacific Rise toward the Garrett Fracture Zone, *J. Geophys. Res.*, **102**, 3097–3108, 1997.
- Tong, C. H., et al., Asymmetric melt sills and upper crustal construction beneath overlapping ridge segments: Implications for the development of melt sills and ridge crests, *Geology*, **30**, 83–86, 2002.
- Toomey, D. R., G. M. Purdy, S. C. Solomon, and W. S. D. Wilcock, The three-dimensional seismic velocity structure of the East Pacific Rise near latitude 9°30'N, *Nature*, **347**, 639–645, 1990.
- Toomey, D. R., S. C. Solomon, and G. M. Purdy, Tomographic imaging of the shallow crustal structure of the East Pacific Rise at 9°30'N, *J. Geophys. Res.*, **99**, 24,135–24,157, 1994.
- Van Avendonk, H. J. A., A. J. Harding, J. A. Orcutt, and J. S. McClain, Contrast in crustal structure across the Clipperton transform fault from travel time tomography, *J. Geophys. Res.*, **106**, 10,961–10,981, 2001.
- Vera, E. E., J. C. Mutter, P. Buhl, J. A. Orcutt, A. J. Harding, M. E. Kappus, R. S. Detrick, and T. M. Brocher, The structure of 0- to 0.2-m.y.-old oceanic crust at 9°N on the East Pacific Rise from expanded spread profiles, *J. Geophys. Res.*, **95**, 15,529–15,556, 1990.
- Zelt, C. A., Modelling strategies and model assessment for wide-angle seismic traveltimes data, *Geophys. J. Int.*, **139**, 183–204, 1999.

P. J. Barton, R. W. Hobbs, and R. S. White, Department of Earth Sciences, Bullard Laboratories, University of Cambridge, Madingley Road, Cambridge, CB3 0EZ, UK.

S. Bazin and S. C. Singh, Laboratoire de Géosciences Marines, Institut de Physique du Globe de Paris, F-75252, Paris Cedex 05, France.

A. J. Harding, G. M. Kent, and J. A. Orcutt, Cecil H. and Ida M. Green Institute of Geophysics and Planetary Physics, Scripps Institution of Oceanography, University of California, San Diego, CA 92093, USA.

J. W. Pye and C. H. Tong, Department of Earth Science and Engineering, Imperial College London, London SW7 2AZ, UK. (ch.tong@imperial.ac.uk)

M. C. Sinha, Southampton Oceanography Centre, University of Southampton, School of Ocean and Earth Science, Southampton SO14 3ZH, UK.